JOM, Vol. 75, No. 10, 2023
https://doi.org/10.1007/s11837-023-06046-4

Correlation of Microstructure and Local Mechanical Properties Along Build Direction for Multi-layer Friction Surfacing of Aluminum Alloys

ZINA KALLIEN,[1,3] MARIUS HOFFMANN,[1,4] ARNE ROOS,[1,5] and BENJAMIN KLUSEMANN[1,2,6]

1.—Solid State Materials Processing, Institute of Materials Mechanics, Helmholtz-Zentrum Hereon, Max-Planck-Straße 1, 21502 Geesthacht, Germany. 2.—Institute for Production Technology and Systems, Leuphana University Lüneburg, Universitätsallee 1, 21335 Lüneburg, Germany. 3.—e-mail: zina.kallien@hereon.de. 4.—e-mail: marius.hoffmann@hereon.de. 5.—e-mail: arne.roos@hereon.de. 6.—e-mail: benjamin.klusemann@hereon.de

The process variant of friction surfacing (FS) depositing multiple layers on top of each other is known as multi-layer friction surfacing (MLFS). Due to the solid-state nature of the process, re-heating is significantly reduced compared to common fusion-based AM techniques. The work gives a detailed and fundamental insight into the microstructure along the MLFS build direction for two different aluminum alloys and different process parameters. Focusing on the grain size distribution and recrystallization ratio, the stacks show a higher degree of recrystallization and finer grains at the interfaces. The observed grain sizes at the interfaces were 2.0 μm (AA5083) and 1.1 μm (AA2024), and 5.8 μm (AA5083) and 3.1 μm (AA2024) at the layer center. For the non-precipitation-hardenable alloy (AA5083), the local microstructural trend could be related to the hardness distribution along the stacks, i.e., a slightly higher hardness at the layer interfaces (95 HV) compared to the layer center (90 HV). The relationship is more complex for precipitation-hardenable alloys (AA2024), which show a rise in hardness between 40 HV0.2 and 45 HV0.2 along the stack height. The effect of subsequent layer depositions on the microstructure and hardness is discussed and a distinctive grain size distribution along the build direction was shown to be a fundamental characteristic.

INTRODUCTION

Friction surfacing (FS) is a solid-state coating technology for similar and dissimilar metallic materials that also shows a strong potential for repair[1] or solid-state additive manufacturing (AM).[2] It can also be used as an assisting process, as for instance presented by Huang et al.[3] for friction stir welding of aluminum and titanium assisted by FS. The variant of FS where multiple layers are deposited on top of each other is known as multi-layer friction surfacing (MLFS), whereas the deposition of every single layer follows the principle of FS. The deposition process is performed by pressing a rotating consumable stud material onto a substrate, which leads to frictional heat at the materials' interface. This results in deformation and plasticization of the stud. A relative translational movement between the plasticized stud and the substrate enables the deposition of the consumable material onto the substrate as a layer. Due to its solid-state nature, the whole process is performed below the materials' melting temperature. FS is feasible for various similar and dissimilar material combinations, where the three main process parameters are rotational speed, axial force, and travel speed. The process parameters affect the deposition, e.g., in terms of process temperature, layer geometry, and efficiency. These effects are discussed in the

(Received May 3, 2023; accepted July 24, 2023; published online August 29, 2023)

literature and were summarized in a review by Gandra et al.[4] However, the phenomena during FS and the relationship of process parameters, temperature, microstructure, and mechanical properties are complex. It was shown by Isupov et al.[5] and verified by Kallien et al.[6] that layer geometry and process temperature are in a direct relationship.

FS deposits show a significantly refined microstructure, as described by Galvis et al.[7] for aluminum and by Damodaram et al.[1] for Inconel. Suhuddin et al.[8] investigated the microstructure in aluminum stud material after layer deposition with the focus on the flash, which is formed by the material that is pressed out of the process zone. The significantly refined microstructure as a result of the FS process showed evidence for continuous and discontinuous recrystallization. The fine-grained recrystallized microstructure of the deposit is characteristic for friction-based layer deposition techniques and has also been observed for wire-based friction stir additive manufacturing[9] or additive friction stir deposition.[10] The principles of both processes are closely related to the FS technique, but require a tool to feed the consumable material. The effect of FS process parameters on the microstructure was investigated by Rahmati et al.[11] for FS deposition of AA2024 on AA1050. The study presented a difference in grain size between the upper and lower parts of the coating which is influenced by the process parameters. For the deposition of AA6061 on carbon steel, Yu et al.[12] found that the grain size decreases with increasing rotational speed. Ehrich et al.[13] investigated the grain size within the FS layer for aluminum alloys with different Mg content. The analysis showed smaller grains at the advancing side (AS) of the deposit compared to retreating side (RS) and center. The deposits with higher Mg content showed smaller grains and a higher fraction of high-angle grain boundaries (HAGB).

Despite the solid-state nature of FS, there remains a recurrent temperature input when MLFS is performed.[14] Although it is lower compared to fusion-based AM techniques, the effect on the resulting microstructural properties of the deposited material still needs to be understood. Shen et al.[15] analyzed the microstructure of a six-layer AA5083 stack built on an AA2024 substrate at constant parameters. No change of average grain size was observed along the stack height and the subsequent layer depositions were found to have no influence on the previously deposited layers. However, this study was limited to analyze only one position per deposit. In contrast, the present study aims for a deeper and fundamental insight into the microstructure along MLFS stacks for different aluminum alloys deposited at varied process parameters. An extensive analysis of the microstructure within the deposited layers along the stack height has been performed using electron backscatter diffraction (EBSD). Additional hardness measurements contribute to a fundamental understanding of the properties of the deposited aluminum structures, which is crucial knowledge in further developing MLFS as solid-state AM technology.

MATERIALS AND METHODS

The MLFS experiments of this study were performed using a custom-designed friction welding system (RAS; Henry Loitz Robotik, Germany) specialized for the FS process. The welding equipment is able to apply process forces up to 60 kN, maximum torques of 200 Nm, and maximum rotational speed of 6000 rpm. The available working area is 1.5 m × 0.5 m × 0.5 m (x, y, z). Each MLFS layer deposition follows the principle of FS. The consumable stud was positioned above a substrate, where defined rotational speed and axial force were applied. As a result, the stud is pressed onto the substrate surface and starts to deform and plasticize (plasticizing phase). The deposition phase starts with superimposing the relative translational movement between the plasticized stud and the substrate at a defined travel speed, enabling the layer deposition. All the experiments were performed force-controlled at room temperature. Between the subsequent layers, there was enough time for the stack to cool to room temperature before the deposition of the following layer was initiated. For each investigated parameter set, the process temperature was measured during the deposition at a distance of 0.5 mm to the substrate interface using three thermocouples of type K (CONATEX Dipl.-Ing. L. Colbus, Germany) inserted in the substrate from the bottom side. The thermocouples were distributed equidistant at a distance of 5 mm from AS to RS.

Two different aluminum alloys were used as consumable stud material (20 mm diameter, 125 mm length) in this study, i.e., the Al-Cu alloy AA2024 T3 and the Al-Mg alloy AA5083 H112. In contrast to AA5083, AA2024 is a precipitation-hardenable alloy and the use of these two alloys allows the investigation of fundamental MLFS characteristics for a non-heat-treatable and a heat-treatable aluminum alloy. All the stacks were built on AA2024 T3 substrates (300 mm length, 150 mm width, 8 mm thickness). A backing plate was used (AA7050 T7451, 12 mm thickness) between the substrate and the machine table. For each stack, five layers were deposited above each other.

The main process parameters are rotational speed, axial force, and travel speed. An overview of the applied process parameters during layer deposition is provided in Table I. The stacks 2024-A and 5083-A were built with similar process parameters in order to compare the behavior of the two different Al alloys. Furthermore, the intention of this study is to compare different layer thicknesses for each Al alloy individually as well as

Table I. Overview of MLFS process parameters used for five-layer stacks, including the resulting average layer thickness and measured maximal process temperature

	Stud material	Axial force, kN	Rotational speed, rpm	Travel speed, mm/s	Average layer thickness, mm	Max. process temperature, °C
5083-A	AA5083	8	1200	6	1.44	387.7
5083-B	AA5083	8	800	4	2.48	366.9
2024-A	AA2024	8	1200	6	0.82	361.5
2024-B	AA2024	8	800	3	1.70	341.7

comparable layer thicknesses for the two different Al alloys by changing the process parameters for the stacks 2024-B and 5083-B. Apart from the layer geometry, the process parameters also affect the stud consumption rate. For this reason, the attainable welding lengths to compare the process parameters with thicker layers (2024-B and 5083-B) to the parameters with thinner layers (2024-A and 5083-A) varied. Consequently, the lengths of the built structures were 210 mm for 2024-A and 5083-A and 160 mm for 2024-B and 5083-B.

In order to analyze the stacks with regard to layer geometry and microstructure, three cross-sections were extracted from each stack at the center along the stack length. The cross-sections were embedded and prepared following common metallographic procedures, i.e., grinding with SiC paper of 800 μm, 1200 μm, 2000 μm, and 4000 μm, followed by polishing with 3 μm and 1 μm diamond paste. Furthermore, the EBSD samples had undergone an overnight vibration polishing step using a Vibro-Met2 vibratory polisher (Buehler, Germany). The macroscopic analysis of the base material (BM) and stack appearance was performed using a light optical microscope (VHX-6000; Keyence, Germany). Micro-hardness measurements were performed at the earliest 4 weeks after the deposition process using a Durascan 70 G5 automated hardness testing machine (EMCO-TEST Prüfmaschinen, Austria) in accordance with DIN EN ISO 6508-1. Measurements were performed with a load of 0.2 kg at a holding time of 10 s, for which a Vickers indenter with a 136° opening angle was used. Seven lines of hardness indents with a distance of 0.15 mm between the indents were performed on each sample, where the average hardness value along the stack-height is shown in the following results. The microstructures were analyzed using a scanning electron microscope Quanta 650 (Thermo Fisher Scientific, USA) equipped with an EDAX EBSD detector of the Velocity series and an EDAX Octane Elect Super energy-dispersive X-ray spectroscopy (EDS) system (both AMETEK, USA). The EBSD data were acquired using 15 kV and a working distance of 16 mm at a step size of 0.2 μm. The $\times$1000 magnification used leads to a total scan area of 174.8 μm $\times$ 136.8 μm. Starting from the layer-to-substrate (LTS) interface, the total scan area was divided into four sections, which were examined with regard to grain size and local misorientation angles (Fig. 1). The scans were performed in specific representative regions along the build direction. The scans were performed in the center of the samples starting at the LTS interface until the third layer as well as the top layer for both aluminum alloys were deposited at similar process parameters (2024-A and 5083-A). The scanning strategy allows seeing possible gradients along the build direction as well as to assess the effect of subsequent deposition processes, as the top layer was investigated and the results could be compared to the other layers. The EBSD scanning of 2024-B and 5083-B was performed in the region of the third layer, as this layer is assumed to be representative for the 5-layer stacks. The analyses were carried out using MTEX toolbox version 5.8.1 in MATLAB (The Mathworks, USA). The minimal grain size was defined as 5 pixels and, in order to define grain boundaries, the misorientation angle of two neighboring grains was set to 5°. Low-angle grain boundaries (LAGB) were defined for misorientation angles between 5° and 15° whereas, after reaching a critical misorientation angle, i.e., 15°, they are considered as HAGB.[16]

For analyzing the recrystallization behavior along the MLFS build direction, the grain orientation spread (GOS) and the ratio of HAGB to LAGB were determined from the EBSD data. With GOS, the averaged local misorientation within a grain to its main orientation can be expressed, i.e., a low GOS value refers to a low deformed microstructure. The critical value to distinguish between recrystallized and non-recrystallized grains varies between 1° and 5°,[17–19] where this investigation uses two different GOS value criteria for comparison, i.e., lower to 2° and lower to 5°. Furthermore, the misorientation analysis by calculating the ratio of HAGB to LAGB is considered as another criterion to determine recrystallization. During continuous dynamic recrystallization, dislocations progressively accumulate in LAGB which lead to an increase of their misorientation.

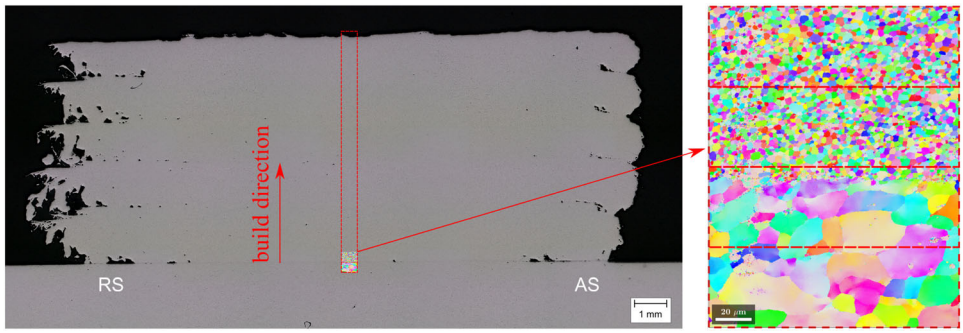

Fig. 1. EBSD scan position in the center of the samples indicated by the red line (left), division of each scan into four subsections (right) (Color figure online).

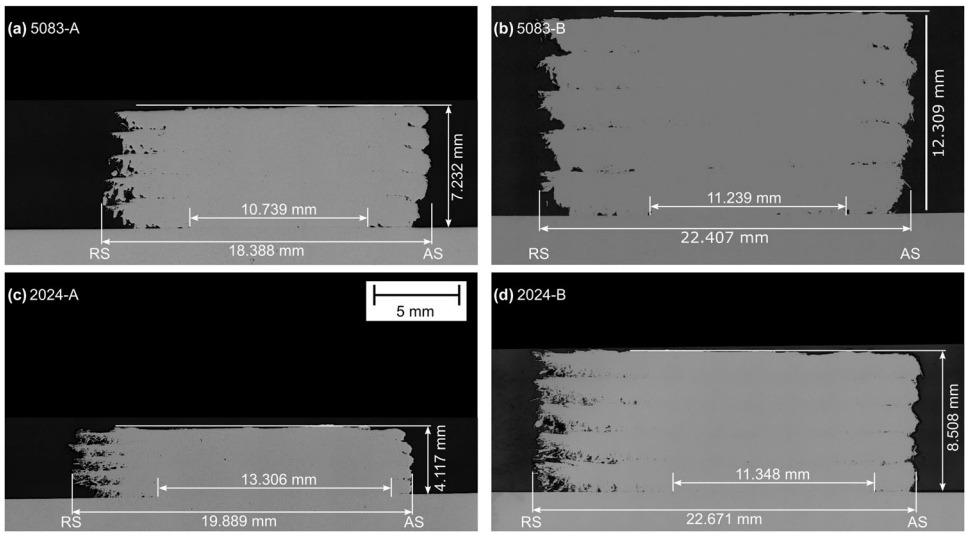

Fig. 2. MLFS stack cross-sections: AA5083/AA2024 stacks on the top (a, b) and AA2024/AA2024 stacks on the bottom (c, d).

RESULTS AND DISCUSSION

Layer Geometry and Process Temperature

Five-layer stacks were built via MLFS using AA5083 as well as AA2024 consumable stud material at process parameters presented in Table I. All the deposition processes showed a stable and repeatable deposition behavior for all the layers and the resulting stacks' cross-sections are illustrated in Fig. 2. The reduction of the rotational and travel speeds for 5083-B and 2024-B led to significantly thicker layers. The effect of process parameters on the deposit geometry has already been investigated for various materials and is not discussed here in depth for brevity. The interested reader is referred to the review by Gandra et al.[4] For the AA5083 consumable stud material, average layer thicknesses of 1.44 mm (5083-A) and 2.48 mm (5083-B) were achieved, whereas the AA2024 consumable stud material led to average layer thicknesses of 0.82 mm (2024-A) and 1.70 mm (2024-B).

At similar process parameters for AA5083 and AA2024 (5083-A and 2024-A), the latter shows significantly thinner deposits. Hanke and dos Santos[20] made similar observations comparing AA5083 and AA6082 using similar process parameters, where the AA6082 stud material resulted in thicker and wider deposits. This aspect is attributed to a higher stud consumption rate, i.e., the speed in the axial direction, and a lower nominal specific energy required for stud consumption of AA6082 compared to AA5083. The nominal specific energy is defined as the ratio of introduced power during the process per consumed stud material volume:[20]

$$e_s = \frac{P_T + P_Z}{\pi \cdot r^2 \cdot v_{CR}} = \frac{2 \cdot \pi \cdot n \cdot T + F_Z \cdot v_{CR}}{\pi \cdot r^2 \cdot v_{CR}}, \qquad (1)$$

with stud radius r as well as torsional power component P_T, dependent on rotational speed n and torque T, and axial power component P_Z, dependent on applied axial Force F_Z and stud consumption rate v_{CR}. In the present investigation, the deposition of AA5083 showed a higher stud consumption rate, i.e., 1.8 mm/s (5083-A) compared to 1.1 mm/s (2024-A), but a similar process torque, i.e., 27.8 Nm (5083-A) and 28.1 Nm (2024-A), which leads to a lower

nominal specific energy, i.e., 31.7 J/mm^3 (5083-A) compared to 35.3 J/mm^3 (2024-A), resulting in more distinct deformation and higher deposited volumes for the AA5083 stud material at constant process parameters. For 5083-B, a stud consumption rate of 1.6 mm/s and a process torque of 37.1 Nm leads to a nominal specific energy of 31.1 J/mm^3. The nominal specific energy for 2024-B is 34.1 J/mm^3, with a stud consumption rate and a process torque of 1.0 mm/s and 33.0 Nm, respectively. Due to the decrease of the rotational and travel speeds, the nominal specific energy decreased for both alloys. The process torque using the same process parameters is nearly the same for AA2024 and AA5083, which correlates with the temperature-dependent yield strength at the temperature during deposition, i.e., between 20 MPa and 40 MPa for both AA2024[21] and AA5083.[22] The thermal conductivity might influence the stud consumption rate, i.e., the higher thermal conductivity for AA2024 leads to a sharper temperature gradient within the stud. Therefore, more stud material has to heat up before it is deposited, resulting in a lower stud consumption rate.

The process temperatures were recorded for all the process parameters in the substrate for a single-layer deposition, assuming that the temperatures in the subsequently deposited layers during MLFS are similar compared to the first layer.[14] The maximum process temperatures are presented in Table I, and the corresponding temperature evolution for the different process parameters is given in Fig. 3. The observed temperatures for 5083-A are higher than those for 2024-A, although the same process parameters have been employed. For both alloys, a decrease of the rotational and travel speeds results in a lower maximum process temperature. However, for a decreased travel speed, the time above a certain temperature, e.g., 250°C, is longer, i.e., 3.34 s (2024-A) and 7.14 s (2024-B).

In the following, the microstructure distribution of both aluminum alloys along the stack is discussed in detail separately, followed by a discussion of the results and a correlation of the observed phenomena with the mechanical properties.

Microstructure AA5083

Grain Size Distribution

The results of the average grain size analyses performed via EBSD along the build direction of the AA5083 stacks are shown in Figs. 4 and 5. A periodic distribution with average grain sizes between 2.0 μm and 5.8 μm is observable for both stacks, where the center of each layer shows a higher average grain size with a larger standard deviation compared to the layer interfaces. The average grain size distribution within the top layer of 5083-A shows a similar distribution. This observation clearly indicates that the smaller average grain size at the layers' interfaces has no effect on further deposition processes, i.e., thermo-mechanical loading due to subsequent layer deposition. This finding is in agreement with Shen et al.[15] The temperature during MLFS of AA5083 at similar process parameters was reported to reach a maximum of approximately 372°C within the third layer during the deposition of the subsequent fourth layer,[14] which is within the range of the observed temperatures in this study.

It is well accepted that the process parameters also affect the grain size, i.e., Rahmati et al.[11] observed a decrease in average grain size for decreasing axial feeding rate, increasing travel speed, and decreasing rotational speed for the FS of AA2024 over AA1050. This change in grain size is associated with the varying plastic strain and

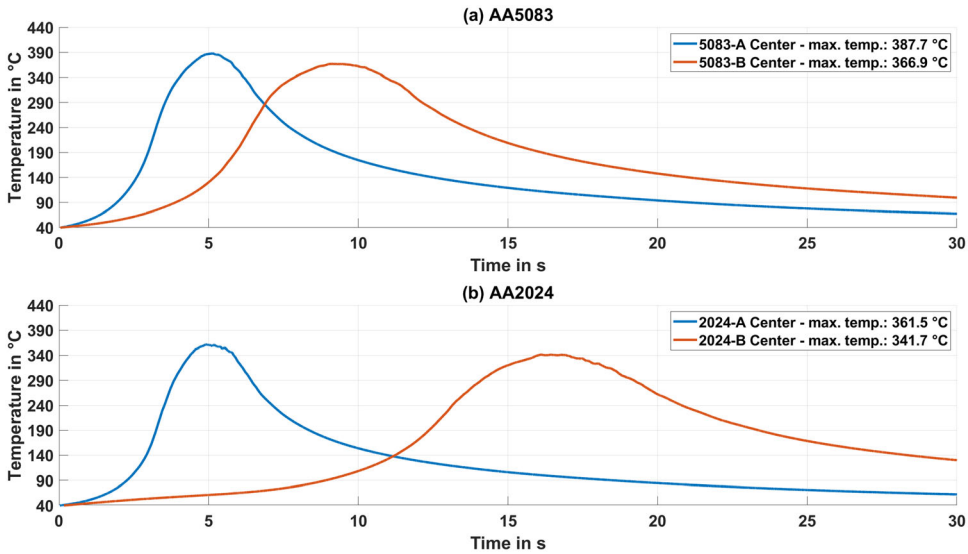

Fig. 3. Temperature evolution for single-layer deposition at different process parameters for AA5083 (a) and AA2024 (b) consumable material.

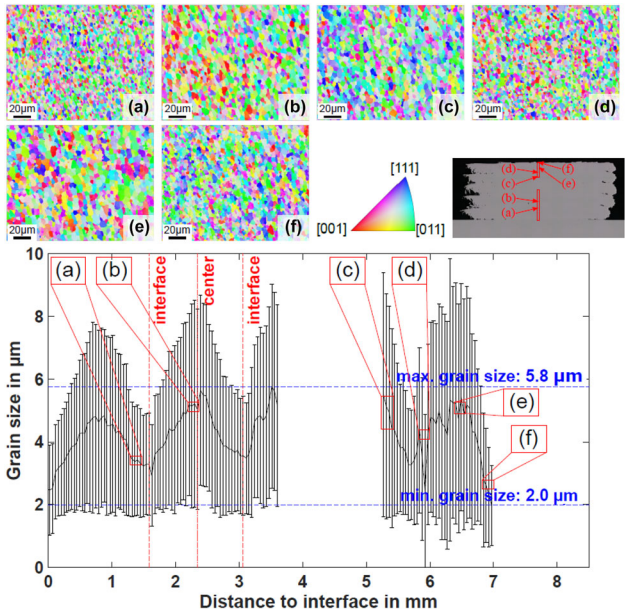

Fig. 4. MLFS 5083-A grain size distribution along the build direction with exemplary inverse pole figure (IPF) maps at the interface (a, d), in the deposit center (b, c, e) and the top layer (f).

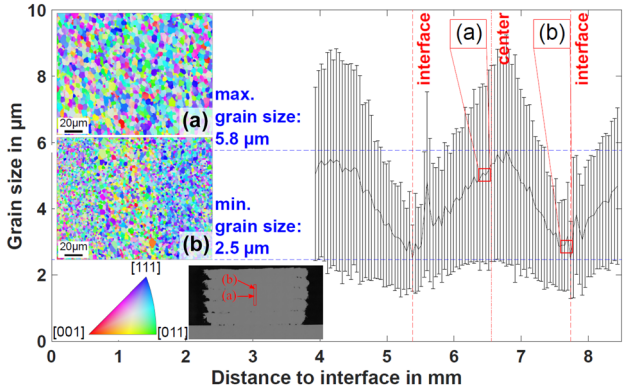

Fig. 5. MLFS 5083-B grain size distribution along the build direction with IPF maps at the deposit center (a) and in the interface (b).

temperature condition for varying process parameters. For the present study, comparing the results of the stacks 5083-A and 5083-B, the change in process parameters, i.e., the reduction of rotational and travel speeds, led to a significant change in deposit geometry, i.e., increase in layer thickness, and an approx. 20°C lower process temperature. However, the change in process parameters had no significant effect on the average grain size distribution along the build direction of the deposited structure (Figs. 4 and 5). Since the characteristic periodic pattern is also present for both parameter combinations, this grain size distribution seems to represent a characteristic of each individual MLFS layer, which is further investigated below.

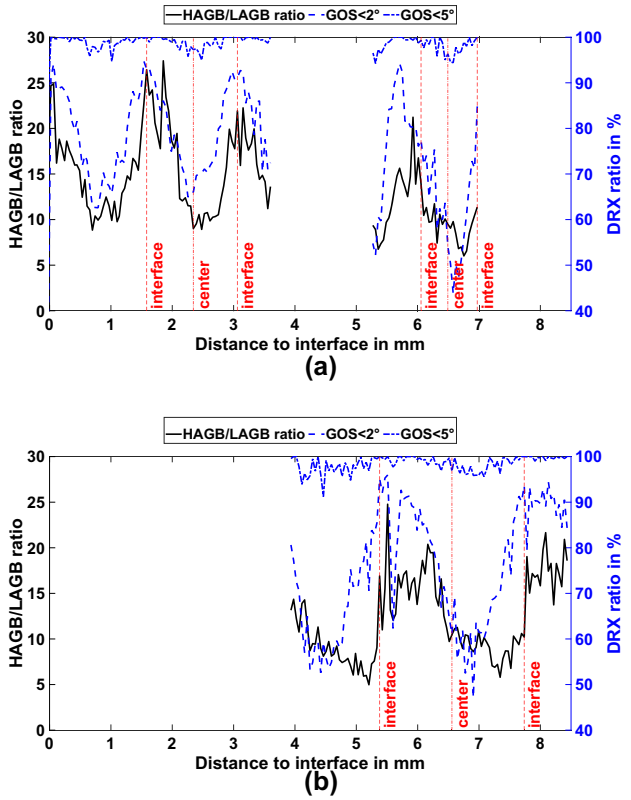

Fig. 6. Ratio of HAGB to LAGB and DRX-ed grains for 5083-A (a) and 5083-B (b).

Recrystallization

Similar to the grain size, the areal fraction of dynamically recrystallized (DRX-ed) grains of both AA5083 stacks show a periodic change with stack height position (see Fig. 6), considering the HAGB/LAGB ratio and the DRX ratio (GOS value lower to 2°). The stacks show increased values close to the interfaces and a decrease to the center of each layer. In 5083-A (Fig. 6a), the DRX ratio (GOS < 2°) is slightly above 90% at the interface and about 65% in the layers' center. The DRX ratio (GOS < 5°) ranges between 95% and 100% with slightly lower values in the center of each layer. This comparison indicates a high amount of grains with a GOS value between 2° and 5° in the layers' center.

Microstructure AA2024

Grain Size Distribution

The results of average grain size distribution in the AA2024 MLFS stacks are shown in Figs. 7 and 8. Similar to the results of AA5083, the AA2024 MLFS stacks show a periodic change in grain size along the build direction, i.e., stack height. The stacks show a minimum grain size in the region of the deposits' interfaces (1.1 μm and 2.0 μm for 2024-A and 2024-B, respectively), and the largest grains were measured approximately in the center of the

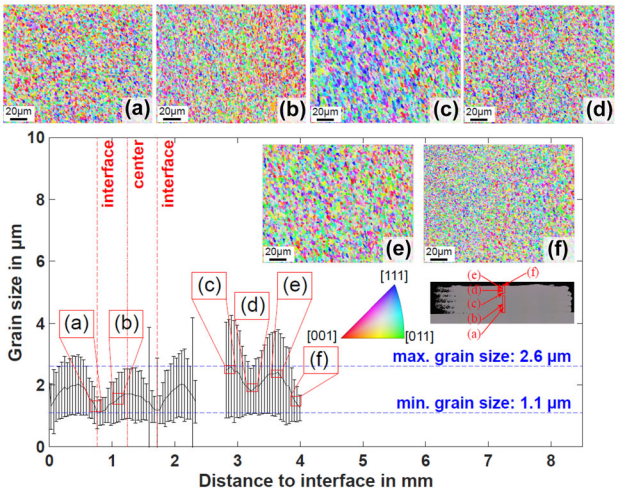

Fig. 7. MLFS 2024-A grain size distribution along the build direction with IPF maps at the interface (a, d), in the deposit center (b, c, e), and top layer (f).

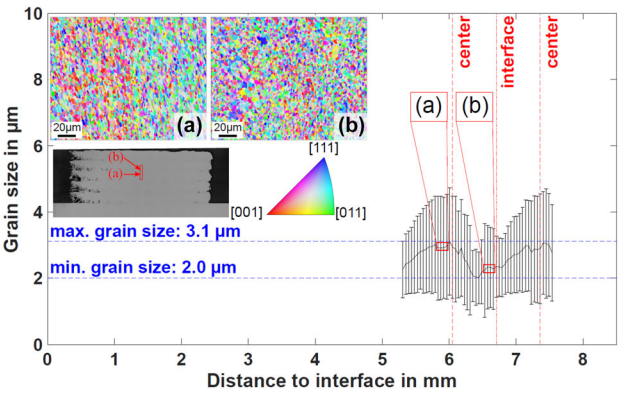

Fig. 8. MLFS 2024-B grain size distribution along the build direction with IPF maps at the deposit center (a) and in the interface (b).

layer (2.6 μm and 3.1 μm for 2024-A and 2024-B, respectively). This distribution can also be observed in the top layer of each AA2024 MLFS stack that has not experienced a further thermo-mechanical processing due to the subsequent layer deposition. The variation of average grain size distribution along the build direction is observable for both alloys at two different process parameters, but less pronounced for the AA2024 consumable material.

Overall, the grains for AA2024 are smaller, which might be a result of the different chemical composition compared to AA5083.[13,20] Ehrich et al.[13] stated that the alloy composition is a crucial factor for grain size and grain boundary ratio for FS deposits. Furthermore, according to Hanke and dos Santos,[20] a lower stud consumption rate leads to higher shear strains, since the stud material remains longer within the shear zone. A higher amount of dissolved foreign atoms, like in AA2024 compared to AA5083, leads to a reduction of stacking fault energy which causes a lower rate of dislocation annihilation,[20] which may also result in a reduction of grain size. Furthermore, the

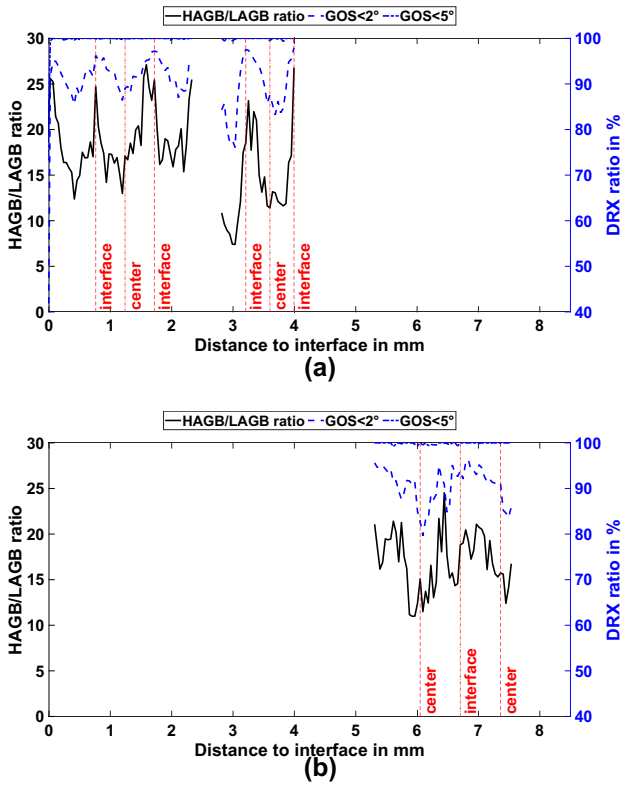

Fig. 9. Ratio of HAGB to LAGB and DRX-ed grains for 2024-A (a) and 2024-B (b).

difference in the chemical composition affects the DRX mechanisms and may contribute to different process behavior.[20] To confirm that there is no local variation in chemical composition at the interface or center regions within the layers, EDS scans were performed for AA5083 and AA2024 for the first two layers and in the fifth layer, as well as in the LTS and at the interfaces between the first and second layers as well as the second and third layers. No significant differences in chemical composition between the layers' center and interface could be observed. In terms of the grain size distribution itself, the results for AA2024 support the findings from AA5083.

Recrystallization

In 2024-A and 2024-B, a similar DRX trend than in the AA5083 MLFS stacks is observed, with DRX ratios (GOS value lower 2°) between 71% and 96% and between 70% and 92%, respectively (Fig. 9). The HAGB/LAGB ratios for 2024-A and 2024-B show the same trend, i.e., decreasing in the center of the layers and increasing in the interface regions, confirming the previous findings in terms of grain size.

Discussion of Underlying Phenomena

Overall, the absolute variation in grain size observed along MLFS stack height is small

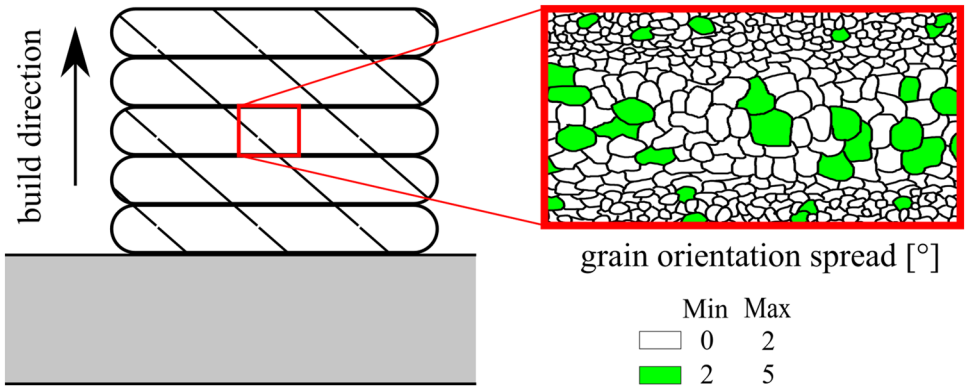

Fig. 10. Summary of discussed observations on the characteristic microstructure along the layer thickness. At the top, the strain rate is assumed to have a dominant effect on the microstructure, where the temperature, i.e., rapid cooling due to heat conduction to the material below, plays a major role for the microstructure at the bottom of the layer. Grain growth is assumed to have an effect in the layer center.

comparing the absolute numbers; however, the tendency for slightly smaller grains at the layer interfaces is clear. The presented results for the AA5083 and AA2024 MLFS-deposited material clearly prove that the periodic distribution of the average grain size within each layer is a unique feature of FS and not a result of the subsequently deposited layer, the individual process parameters, or the chemical composition. However, temperature control during the deposition process, e.g., by active cooling, might affect the grain size distribution of an MLFS structure. In the following, a hypothesis for the possible underlying mechanisms is given. For FS, several phenomena are mentioned in the literature[11,13,23] describing the influence on recrystallization behavior and final grain size after recrystallization, e.g., material flow, local strain rates, and temperature evolution, which are most likely in complex interaction with each other, depending on the chosen process parameters and material composition. Using a powder marker material inside the studs, Belei et al.[23] showed that material flow during FS layer deposition is complex and likely to show a gradient along the layer thickness as well as the width. With regard to possible variations along the layer thickness, Rahmati et al.[11] showed that the grain size of FS-deposited material decreases from top to bottom. In contrast, in the investigated MLFS stacks within this study, the top and bottom of the layers show finer grains compared to the center, which correlates with the higher ratio of recrystallization in these areas. This can be related to the fact, that recrystallization behavior and the grain size depend on temperature and strain rate,[24] which are not constant within the deposited layer. Pirhayati and Aval[25] showed in a numerical simulation that both strain rate and temperature decrease from top to bottom within a single layer. This implies that the highest strain rate occurs at the material interface between the deposited layer material and the stud material; therefore, a high ratio of recrystallization and smaller grains are expected. This leads to the hypothesis that the effect of strain rate is assumed to be dominant in this region of the layer. In contrast, the bottom of the layer material is assumed to show the highest cooling rate, as the heat is transferred to the substrate or previously deposited material by conduction more quickly. This indicates a shift in dominance from strain rate to temperature in the lower part of the layer close to the interfaces, yielding to a lower average grain size in the bottom part of the layers (Fig. 10).

Considering the DRX criteria of the HAGB/LAGB ratio and a GOS value lower than 2°, a higher degree of DRX was observed at the layers' interfaces, where the observed trend was more distinct for the thicker layer of AA5083. Considering the criterion of a GOS value lower than 5°, the layer center presents a high fraction of grains presenting a GOS value between 2° and 5°. Grains with a GOS value lower than 2° are considered as recently recrystallized, whereas a GOS value between 2° and 5° represents recrystallized and deformed grains, i.e., grains that recrystallized at an earlier stage of deformation during the process.[26] This observation indicates that almost the whole microstructure experienced recrystallization over the whole stack height, where more grain growth might have occurred afterwards in the center region of each layer. This conclusion holds for all investigated stacks, independent of the stud material, specific layer geometry, and process parameters.

Correlation with Hardness

The hardness measurements for all the stacks are presented in Fig. 11. The hardness measurements for the non-heat-treatable AA5083 material show a constant periodic distribution correlating well with the layer thickness. The measured hardness in the top and bottom parts of the layers is slightly higher compared to the center. This observation is also valid for the top layer that has not been affected by a further MLFS deposition process. Overall, the values are in the range of the AA5083 H112 stud BM (BM hardness measurement: 93 ± 6 HV0.2). As a

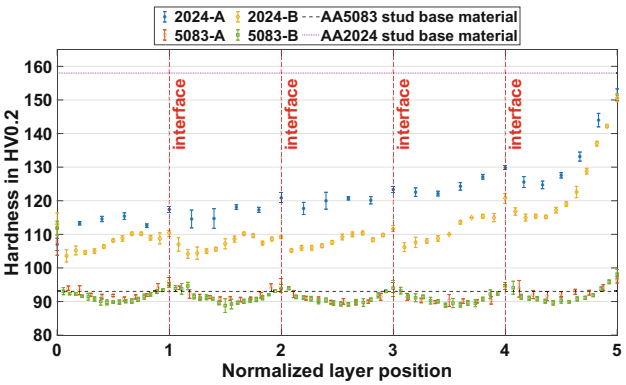

Fig. 11. Comparison of hardness (HV0.2) along the height of the five-layer MLFS stacks for all the investigated process parameters of this study. For comparison purposes, the positions within the layers are normalized.

non-heat-treatable, the strength of AA5083 mainly depends on the elements in solid solution and the grain size.[27] Since no change in chemical composition within the layer is present, the change in hardness can be directly attributed to the Hall–Petch effect,[28] where smaller grains at the interfaces show a slightly higher hardness compared to the center of the deposited layers.

In terms of the precipitation-hardenable AA2024, additional phenomena influence the hardness distribution. The hardness measurements of the AA2024 T3 stud BM revealed a value of 158 ± 7 HV0.2. In contrast to the AA5083 MLFS structures, the AA2024 layer material shows a rise in hardness along the build direction (Fig. 11). The hardness distribution within each layer is also periodic; however, a steady increase in hardness can be observed along the stack height, where a very pronounced increase is visible towards the top layer. A similar observation was reported by Gandra et al.[29] for the MLFS AA6082 consumable stud material; however, no significant grain size variation between the deposited layers was presented. The temperature input induced by subsequent deposition led to an over-ageing of the previous layers.[29] The significant increase of hardness at the top of the AA2024 stacks can be attributed to the fact that the top layer was not affected by a subsequent deposition, like the layers below. Subsequent depositions result in subsequent thermo-mechanical cycles and, as a result, dissolution and (trans-)formation or coarsening of the precipitates. Despite the fact that the hardness for 2024-A compared to 2024-B is slightly higher, the hardness at the top of the fifth layer is the same (≈ 150 HV0.2) and comparable to the stud BM (158 ± 7 HV0.2). The slightly lower hardness observed for 2024-B might be an effect of the chosen process parameters. Compared to 2024-A, the travel speed is lower, which leads to a longer process duration at high temperatures (Fig. 3) and therefore different precipitation kinetics. In the temperature range between 300°C and 470°C, the precipitates with the highest strengthening contribution, i.e., S' (Al_2CuMg)/Θ' (Al_2Cu), dissolve or transform to S/Θ precipitates.[30] This temperature region is reached for 2.36 s (2024-A) and 4.44 s (2024-B). Furthermore, 2024-B exhibits a higher average grain size, which also affects the stack hardness due to the Hall–Petch effect. These two effects are assumed to be responsible for the lower hardness observed in 2024-B compared to 2024-A.

Additionally, the heat input during subsequent depositions might cause changes of the precipitation in the previously deposited layers. Genevois et al.[31,32] investigated the precipitation behavior, i.e., the volume fraction of S precipitates and the Guinier–Preston–Bagaryatskii (GPB) zones, and its influence on the weld cross-section hardness for AA2024 in friction stir welding (FSW) for BM in T351 and T6 temper condition. The GPB zones were identified as the strengthening precipitates in the T351 BM, while no S phase was detected. In the stir zone (SZ), the highest process temperatures and strain values were reached during FSW, which led to dissolution of the S phase precipitates. After the welding process, new GPB zones were formed at room temperature due to natural ageing, leading to a higher hardness. These precipitation mechanisms are also expected to take place during the FS process. To draw an analogy between FS and FSW, the top layer can be seen as the SZ where the highest process temperatures prevail, and, consequently, the highest hardness is measured due to the formation of GPB zones, which agrees with the observation of Ehrich et al.[30] for an AA2024 FS single layer. In the MLFS stacks, the underlying layers experience recurring heating processes with temperatures below the maximum temperature, resulting in a dissolution of the GPB zones and a growth of precipitates, resulting in a hardness decrease in the lower layers of the MLFS stack. For 2024-B, especially, the lower travel speed results in a longer re-heating phase of the previously deposited layers, as already described above, which might lead to GPB zone dissolution and a more pronounced S'/Θ' to S/Θ transformation than in 2024-A. The results show that the specific chemical composition of the aluminum alloy has a considerable effect on the mechanical properties of the MLFS build structure. However, the characteristic distribution in terms of grain size and DRX ratio seems to be independent from phenomena such as precipitation hardening.

CONCLUSION

Extensive microstructure analyses of MLFS-deposited structures using EBSD for two different Al alloys have shown that fundamental microstructural phenomena can be observed independent of the alloy used. The major findings can be summarized as:

- Periodic variation in the average grain size along the MLFS build direction was observed for different Al alloys, where slightly finer grains and higher recrystallization ratios are observable at the layers' interfaces. The observed grain sizes at the interfaces were 2.0 μm (AA5083) and 1.1 μm (AA2024), and 5.8 μm (AA5083) and 3.1 μm (AA2024) at the layers' center.
- For the process setup investigated, the observed average grain size distribution is a fundamental characteristic of a FS layer and no significant effect due to subsequent thermo-mechanical processing, i.e., deposition of further layers via MLFS, could be observed.
- The observed microstructure distribution can be attributed to the varying strain and temperature conditions during the FS layer deposition with a dominance of strain rate and temperature gradient in the layers' top region and in the bottom part, respectively. Furthermore, grain growth might be present in the layers' center.
- The microstructure was set in direct relation with the hardness distribution for non-precipitation-hardenable AA5083, where slightly higher hardness can be observed at the layers' interfaces. The hardness values for the AA5083 at the interfaces and in the layer center were 95 HV0.2 and 90 HV0.2, respectively.
- The precipitation-hardenable AA2024 showed a hardness increase of 40–45 HV0.2 from the first layer to the fifth layer along the stack height. This observation is likely to be a result of the subsequent thermo-mechanical loading of previously deposited material during MLFS, leading to precipitation dissolution and growth.

AUTHOR CONTRIBUTIONS

Conceptualization: ZK, MH; methodology: ZK, MH; validation: ZK, MH; formal analysis: ZK, MH; investigation: ZK, MH; resources: BK; data curation: ZK, MH; writing-original draft: ZK, MH; writing-review & editing: ZK, MH, AR, BK; visualization: ZK, MH; supervision: AR, BK; funding: BK

FUNDING

Open Access funding enabled and organized by Projekt DEAL. This project has received funding from the European Research Council (ERC) under the European Unions Horizon 2020 research and innovation programme (Grant Agreement No. 101001567).

DATA AVAILABILITY

The obtained data of this research is online available at Zenodo (https://doi.org/10.5281/zenodo.8245510).

CONFLICT OF INTEREST

The authors have no relevant financial or non-financial interests to disclose.

OPEN ACCESS

REFERENCES

1. R. Damodaram, P. Rai, S.C.J. Daniel, R. Bauri and D. Yadav, *Surf. Coat. Technol.* (2021). https://doi.org/10.1016/j.surfcoat.2021.127482.
2. J.J.S. Dilip, S. Babu, S.V. Rajan, K.H. Rafi, G.D. JanakiRam and B.E. Stucker, *Mater. Manuf. Process.* (2013). https://doi.org/10.1080/10426914.2012.677912.
3. Y. Huang, Z. Lv, L. Wan, J. Shen and J.F. dos Santos, *Mater. Lett.* (2017). https://doi.org/10.1016/j.matlet.2017.07.081.
4. J. Gandra, H. Krohn, R.M. Miranda, P. Vilaça, L. Quintino and J.F. Dos Santos, *J. Mater. Process. Technol.* (2014). https://doi.org/10.1016/j.jmatprotec.2013.12.008.
5. F.Y. Isupov, O. Panchenko, L. Zhabrev, I. Mushnikov, E. Rylkov and A.A. Popovich, *Key Eng. Mater.* (2019). https://doi.org/10.4028/www.scientific.net/KEM.822.737.
6. Z. Kallien, L. Rath, A. Roos and B. Klusemann, *Surf. Coat. Technol.* (2020). https://doi.org/10.1016/j.surfcoat.2020.126040.
7. J.C. Galvis, P. Oliveira, M.F. Hupalo, J.P. Martins and A. Carvalho, *J. Mater. Process. Technol.* (2017). https://doi.org/10.1016/j.jmatprotec.2017.02.016.
8. U. Suhuddin, S. Mironov, H. Krohn, M. Beyer and J.F. Dos Santos, *Metall. Mater. Trans. A* (2012). https://doi.org/10.1007/s11661-012-1345-8.
9. H. Chen, X. Meng, J. Chen, Y. Xie, J. Wang, S. Sun, Y. Zhao, J. Li, L. Wan and Y. Huang, *Addit. Manuf.* (2023). https://doi.org/10.1016/j.addma.2023.103557.
10. C.J.T. Mason, R.I. Rodriguez, D.Z. Avery, B.J. Phillips, B.P. Bernarding, M.B. Williams, S.D. Cobbs, J.B. Jordon and P.G. Allison, *Addit. Manuf.* (2021). https://doi.org/10.1016/j.addma.2021.101879.
11. Z. Rahmati, H. JamshidiAval, S. Nourouzi and R. Jamaati, *Mater. Chem. Phys.* (2021). https://doi.org/10.1016/j.matchemphys.2021.124756.
12. M. Yu, H. Zhao, Z. Zhang, L. Zhou, X. Song and N. Ma, *J. Mater. Process. Technol.* (2021). https://doi.org/10.1016/j.jmatprotec.2020.117005.
13. J. Ehrich, A. Roos, B. Klusemann and S. Hanke, *Mater. Sci. Eng. A* (2021). https://doi.org/10.1016/j.msea.2021.141407.
14. Z. Kallien, A. Roos and B. Klusemann, *Key Eng. Mater.* (2022). https://doi.org/10.4028/p-s43q63.

15. J. Shen, S. Hanke, A. Roos, J.F. Dos Santos and B. Klusemann, *AIP Conf. Proc.* (2019). https://doi.org/10.1063/1.5112691.
16. S. Gourdet and F. Montheillet, *Mater. Sci. Eng. A* (2000). https://doi.org/10.1016/S0921-5093(00)00733-4.
17. S. Ding, S. AlamKhan and J. Yanagimoto, *Mater. Sci. Eng. A* (2020). https://doi.org/10.1016/j.msea.2020.139522.
18. S. Ding, S. AlamKhan and J. Yanagimoto, *Mater. Sci. Eng. A*. (2021). https://doi.org/10.1016/j.msea.2021.141673.
19. L. Chen, J. Zhang, J. Tang, G. Chen, G. Zhao and C. Zhang, *J. Mater. Process. Technol.* (2018). https://doi.org/10.1016/j.jmatprotec.2018.05.003.
20. S. Hanke and J.F. dos Santos, *J. Mater. Process. Technol.* (2017). https://doi.org/10.1016/j.jmatprotec.2017.04.021.
21. MatWeb—Material Property Data: Aluminum 2024-T3 (2022). https://www.matweb.com/search/DataSheet.aspx?MatGUID=57483b4d782940faaf12964a1821fb61. Accessed 05 Jul 2023.
22. Z. Kallien, A. Roos, C. Knothe-Horstmann and B. Klusemann, *Mater. Sci. Eng. A* (2023). https://doi.org/10.1016/j.msea.2023.144872.
23. C. Belei, V. Fitseva, J.F. Dos Santos, N.G. Alcântara and S. Hanke, *Surf. Coat. Technol.* (2017). https://doi.org/10.1016/j.surfcoat.2017.09.050.
24. T. Sakai and J.J. Jonas, *Acta Metall.* (1984). https://doi.org/10.1016/0001-6160(84)90049-X.
25. P. Pirhayati and H.J. Aval, *Surf. Coat. Technol.* (2020). https://doi.org/10.1016/j.surfcoat.2020.126496.
26. A. Hadadzadeh, F. Mokdad, M.A. Wells and D.L. Chen, *Mater. Sci. Eng. A* (2018). https://doi.org/10.1016/j.msea.2017.10.062.
27. Ø. Ryen, B. Holmedal, O. Nijs, E. Nes, E. Sjölander, H.-E. Ekström, Metall. Mater. Trans. A 37(6) (2006).
28. R.W. Armstrong, *Mater. Trans.* (2014). https://doi.org/10.2320/matertrans.MA201302.
29. J. Gandra, P. Vigarinho, D. Pereira, R.M. Miranda, A. Velhinho and P. Vilaça, *Mater. Des.* (2013). https://doi.org/10.1016/j.matdes.2013.05.059.
30. J. Ehrich, P. Staron, A. Karkar, A. Roos and S. Hanke, *Adv. Eng. Mater.* (2022). https://doi.org/10.1002/adem.202201019.
31. C. Genevois, D. Fabrègue, A. Deschamps and W.J. Poole, *Mater. Sci. Eng. A* (2006). https://doi.org/10.1016/j.msea.2006.07.151.
32. C. Genevois, A. Deschamps, A. Denquin and B. Doisneau-cottignies, *Acta Mater.* (2005). https://doi.org/10.1016/j.actamat.2005.02.007.